Chirality dependent photon transport and helical superradiance

Jonah S. Peter [1,2,*] Stefan Ostermann [1] and Susanne F. Yelin [1]
[1]*Department of Physics, Harvard University, Cambridge, Massachusetts 02138, USA*
[2]*Biophysics Program, Harvard University, Boston, Massachusetts 02115, USA*

(Received 15 November 2023; accepted 20 March 2024; published 22 May 2024; corrected 20 August 2024)

Chirality, or handedness, is a geometrical property denoting a lack of mirror symmetry. Chirality is ubiquitous in nature and is associated with the nonreciprocal interactions observed in complex systems ranging from biomolecules to topological materials. Here, we demonstrate that chiral arrangements of dipole-coupled atoms or molecules can facilitate the helicity-dependent superradiant emission of light. We show that the collective modes of these systems experience an emergent spin-orbit coupling that leads to chirality-dependent photon transport and nontrivial topological properties. These phenomena are fully described within the electric dipole approximation, resulting in very strong optical responses. Our results demonstrate an intimate connection between chirality, superradiance, and photon helicity and provide a comprehensive framework for studying electron transport dynamics in chiral molecules using cold atom quantum simulators.

DOI: 10.1103/PhysRevResearch.6.023200

I. INTRODUCTION

Chirality, or handedness, is ubiquitous in nature and can be observed in macromolecular structures like DNA, down to the single particle level as in photons with circular polarization. An object is chiral if it cannot be superimposed on its mirror image by a rotation. This property allows chiral systems to facilitate nonreciprocal interactions owing to the broken mirror symmetry. Recently, chirality has emerged as an important component to realizing room-temperature spintronics devices via the chirality-induced spin selectivity (CISS) effect [1–5]. Precise control over the transport of helical electrons in chiral molecules and chiral crystals via the CISS effect has promising applications for magnetless spin memories, spin-based logic gates, and other information technologies [6–12]. The interplay between geometrical chirality and the electron spin has also generated interest in fields as diverse as electrochemistry [13,14], molecular biology [15,16], and studies on biological homochirality and the origin of life [8,17].

Of course, in addition to electrons, photons can also carry spin angular momentum, which is encoded in their two orthogonal polarizations [18–21]. The coupling of photons to atoms or molecules [22,23] can result in efficient energy transfer [24–27] and cooperative dissipation leading to the superradiant and subradiant emission of light [28–31]. Demonstration of chirality-induced *photon* transport could facilitate a similar explosion in the development of polarization-controllable photonics devices that are analogous to CISS-based spintronics. The study of dissipative chiral light-matter interactions in a well-controlled setting could also contribute to the study of photoexcitation lifetimes in chiral molecules, which are crucial for various biological processes [32–36].

In this paper, we demonstrate that chiral arrangements of atoms or molecules can facilitate the helicity-dependent superradiant emission of light: an effect we call helical superradiance [Fig. 1(a)]. This phenomenon—which is fully described within the electric dipole approximation—results from an emergent spin-orbit coupling (SOC) that is unique to chiral geometries. We show that the collective excitations of these chiral systems are symmetry-protected helical modes that persist even in the presence of dissipation. Such helicity-dependent chiral transport is associated with a non-Abelian gauge field [37] that results in an excitation band structure with nontrivial topology. Although previous studies have investigated topological properties within photonics systems [38–44], to the best of our knowledge, none have explored the connection between geometrical chirality and superradiant photon emission. These effects may contribute to chiral molecular processes in nature and provide a comprehensive framework for studying the CISS effect in chiral molecules using cold atom quantum simulators.

II. HELICITY DEPENDENT DYNAMICS

Excitation transport between atoms or molecules can be modeled as a collection of quantum emitters interacting with a radiation field [46]. As a minimal model, we focus on a helix as the archetypal chiral geometry—though our results are generalizable to arbitrary chiral setups. The individual dipoles along the helix are modeled as V-type quantum emitters, each with two hyperfine transitions excited by left (σ^+) and right (σ^-) circularly polarized light, respectively, and resonance frequency $\omega_0 = 2\pi c/\lambda_0$, where λ_0 is the wavelength of the optical transition and c is the speed of light in vacuum [Fig. 1(b)]. Long-range dipole-dipole interactions between emitters at positions $\mathbf{r}_i$ and $\mathbf{r}_j$ are mediated through

*jonahpeter@g.harvard.edu

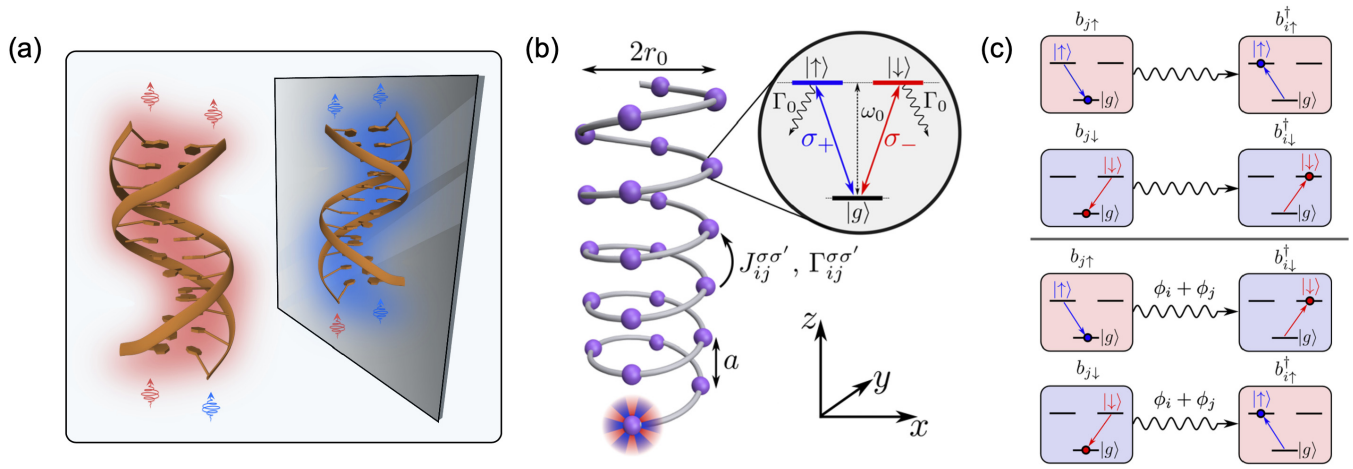

FIG. 1. (a) Illustration of the main results of this paper. Photons with a given helicity (red or blue) are preferentially radiated by structures of a given chirality, leading to helical superradiance [45]. (b) The model used to describe the transport dynamics. Purple spheres denote emitters with a V-type level structure and spontaneous emission rate Γ_0. The lattice geometry is a helix with radius r_0, pitch a, and $\mathcal{N}$ atoms per 2π turn. Emitters are coupled with coherent ($J_{ij}^{\sigma\sigma'}$) and dissipative ($\Gamma_{ij}^{\sigma\sigma'}$) hopping rates. The multicolored halo denotes initialization in an unpolarized mixed state. (c) Interactions between emitters i and j are mediated through photon exchanges that excite orbitals with either the same (top) or opposite (bottom) polarization.

real and virtual photon exchanges that couple orbitals $|\sigma_i\rangle$ and $|\sigma_j'\rangle$ with either the same or opposite polarization. When the photon polarization is changed, conservation of angular momentum requires that the interaction picks up an additional position-dependent phase [Fig. 1(c)]. After tracing out the field degrees of freedom in the Born and Markov approximations [22,23,30,47–49], this system can be described as a collection of pseudospin-1/2 bosons via the Hamiltonian [42]

$$H = \sum_{i=1}^{N}\sum_{\sigma}\omega_0 b_{i\sigma}^\dagger b_{i\sigma} + \sum_{i,j\neq i=1}^{N}\sum_{\sigma,\sigma'} J_{ij}^{\sigma\sigma'} b_{i\sigma}^\dagger b_{j\sigma'} \qquad (1)$$

(we set $\hbar \equiv 1$ here and throughout this work). Here, $b_{i\sigma}^\dagger$ ($b_{i\sigma}$) creates (annihilates) an excitation at site i with spin $\sigma \in \{\uparrow, \downarrow\}$, N is the total number of emitters, and $J_{ij}^{\sigma\sigma'}$ are the spin-dependent hopping rates.

In addition to the coherent interactions described by Eq. (1), we also consider collective dissipation that arises through coupling to the electromagnetic vacuum. In the low-light limit where there is at most a single-excitation in the system at any given time, the full open system dynamics are described by the non-Hermitian effective Hamiltonian:

$$H_{\text{eff}} = H - i\sum_{i,j=1}^{N}\frac{\Gamma_{ij}^{\sigma\sigma'}}{2} b_{i\sigma}^\dagger b_{j\sigma'}. \qquad (2)$$

The anti-Hermitian part of Eq. (2) describes cooperative decay to the vacuum with rates $\Gamma_{ij}^{\sigma\sigma'}$ and single-emitter spontaneous emission with rate $\Gamma_0 \equiv \Gamma_{ii}^{\sigma\sigma}$. In free space, the couplings are determined by the electromagnetic Green's tensor $\mathbf{G}(\mathbf{r}_i - \mathbf{r}_j)$ as

$$J_{ij}^{\sigma\sigma'} - \frac{i}{2}\Gamma_{ij}^{\sigma\sigma'} = -\frac{3}{2}\lambda_0\Gamma_0\hat{\varepsilon}_\sigma^\dagger \cdot \mathbf{G}(\mathbf{r}_i - \mathbf{r}_j)\cdot\hat{\varepsilon}_{\sigma'}, \qquad (3)$$

where $\hat{\varepsilon}_{\uparrow\downarrow} = (\hat{\mathbf{x}} \pm i\hat{\mathbf{y}})/\sqrt{2}$ denote the unit vectors of circular polarization (Appendix A). The time evolution of a general state $\rho(t)$ is then governed by the no-jump quantum master equation, $\dot{\rho} = -i(H_{\text{eff}}\rho - \rho H_{\text{eff}}^\dagger)$.

To illustrate the dynamics, we consider left- (denoted by $\xi = 1$) and right- ($\xi = -1$) handed helices oriented along the z axis with radius r_0, pitch a, $\mathcal{N}$ emitters per 2π turn, and $M = N/\mathcal{N}$ turns total. The initial state is chosen as $\rho(0) = \frac{1}{2}(|\uparrow_i\rangle\langle\uparrow_i| + |\downarrow_i\rangle\langle\downarrow_i|)$, corresponding to an unpolarized statistical mixture of up and down spins localized to a single emitter at $\mathbf{r}_i$. Figure 1(d) shows the total population summed across all emitters in each spin manifold, $P_\sigma(t) = \sum_i P_{i\sigma}(t) = \sum_i \langle b_{i\sigma}^\dagger b_{i\sigma}\rangle$, as a function of time. The top (bottom) two panels show the dynamics when the starting emitter is located at the bottom (top) of the helix. The spin of each state is given by the expectation value $\langle\mathcal{S}_z\rangle$ where $\mathcal{S}_z = \mathbb{1}_N \otimes \sigma_z = \sum_i (b_{i\uparrow}^\dagger b_{i\uparrow} - b_{i\downarrow}^\dagger b_{i\downarrow})$, $\mathbb{1}_N$ is the $N \times N$ identity matrix, and σ_z is the third Pauli operator. As the initial spin wave propagates through the helix with group velocity $\mathbf{v} = v\hat{\mathbf{z}}$ (black arrows), it acquires a helicity, $\eta = \langle\mathcal{S}_z\rangle v/|\langle\mathcal{S}_z\rangle v| = \pm 1$. For the left-handed chirality [left-hand panels of Fig. 1(d)], the positive helicity states [i.e., spin $\uparrow$ ($\downarrow$) propagating upwards (downwards)] experience enhanced dissipation. By contrast, for the right-handed chirality [right-hand panels of Fig. 1(d)], enhanced dissipation occurs with the negative helicity states [spin $\downarrow$ ($\uparrow$) propagating upwards (downwards)]. In both cases, the product $\chi \equiv \xi\eta = -1$ describes configurations with enhanced photoexcitation lifetimes. Figure 1(e) shows a snapshot of the individual emitter populations when the initial upward-moving wave packet reaches the top end of the helix [time $t = \tau$, denoted by dashed lines in Fig. 1(d)]. For the left-handed helix, spin $\downarrow$ excitations exhibit longer lifetimes and are more efficiently transported to the opposite end. The same initial condition results in the preferential transport of spin $\uparrow$ excitations for the right-handed helix. For the more general case when the initial state is an *unequal* statistical mixture of spins, the same dynamics result in the predominant excitation of only one chirality (Appendix B and Fig. 7).

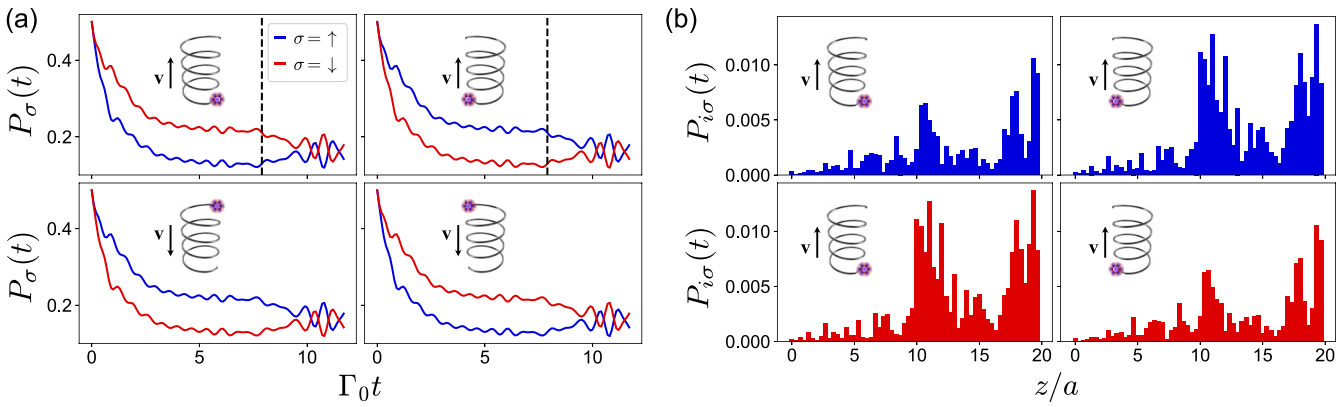

FIG. 2. (a) Population dynamics for left-handed (left-hand panels) and right-handed (right-hand panels) helices after initialization at either the bottom (top two panels) or top (bottom two panels) of the helix. Blue (red) curves denote the total population in the ↑ (↓) manifold as a function of time. Black arrows denote the propagation direction of the initial wave packet. Dashed lines indicate the time $t = \tau$ at which the wave packet reaches the opposite end of the helix. (b) Snapshots of the individual emitter populations at the time denoted in (a). Blue (red) bars denote the spin ↑ (↓) populations of each emitter along the longitudinal helical axis. Parameters for both panels: $r_0 = 0.05\lambda_0$, $a = 0.175\lambda_0$, $\mathcal{N} = 3$, $M = 20$, and $\tau = 7.9/\Gamma_0$.

The magnitude of this chiral transport can be quantified by the spin polarization,

$$\Delta = \int_0^\tau dt \frac{P_\uparrow(t) - P_\downarrow(t)}{P_\uparrow(t) + P_\downarrow(t)}, \tag{4}$$

defined as the difference in population between the spin manifolds integrated until the wave packet reaches the opposite end of the helix at time τ. The transport time is monitored by discretizing the helix into chunks of $N/10$ emitters, and we define τ as the time at which the total emitter population is largest in the final chunk. Figure 3(a) shows the value of Δ for helices of varying radius and pitch. Extremely large spin polarizations—upwards of 40%—are easily achievable across a wide parameter range. A reflection $\mathcal{R}_{yz}$ through the y-z plane preserves the direction of motion but transforms the left-handed lattice geometry to its right-handed mirror image. For any given geometry, the spin polarization is equal and opposite between the left- and right-handed helices. Interestingly, for fixed chirality ξ, both the magnitude and sign of the spin polarization depend nontrivially on the geometric proportions of the helix. This fact may be traced back to the nontrivial positional dependence of the electromagnetic Green's tensor and to the presence of long-range all-to-all couplings that introduce multiple frequency scales to the dynamics (Appendix A and Fig. 6). A rotation $R_x(\pi)$ by an angle π about the x axis preserves the chirality of the helix while changing the sign of both the spin polarization and the direction of propagation. The simultaneous reversal of the spin polarization together with the change in propagation direction demonstrates chirality-dependent SO coupling. Notably, this

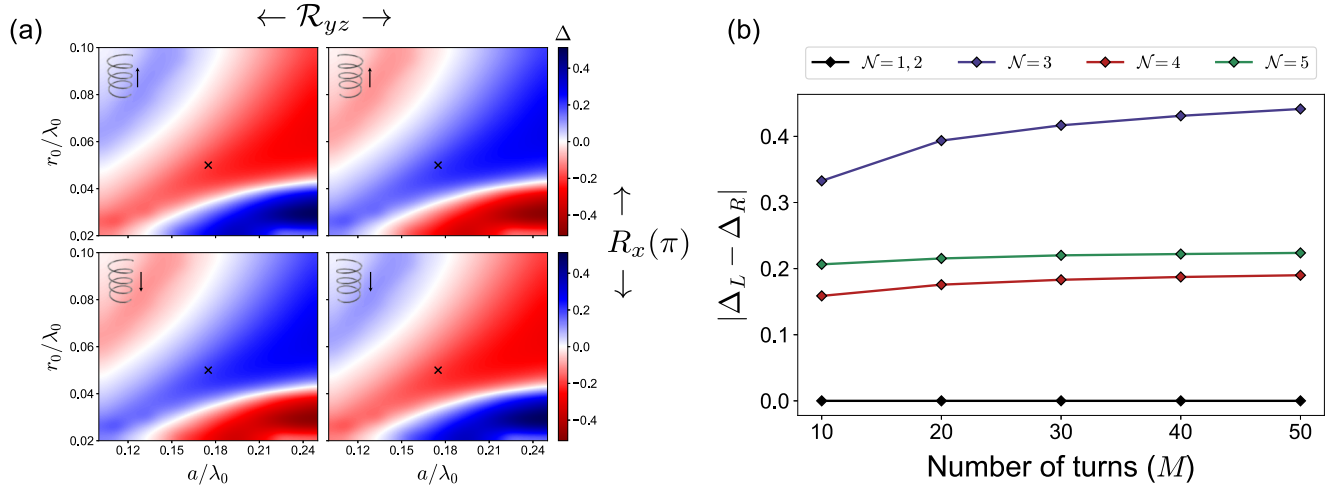

FIG. 3. (a) Spin polarization as a function of helix radius and pitch. Colors show the spin polarization Δ calculated for left-handed (left) and right-handed (right) helices, related by a reflection $\mathcal{R}_{yz}$ through the y-z plane. A rotation $R_x(\pi)$ by an angle π about the x axis reverses the spin polarization and the direction of motion (black arrows). Black crosses denote the radius and pitch used in Fig. 2. Additional parameters: $\mathcal{N} = 3$, $M = 20$. (b) Dependence of the spin polarization on helix length and the number of emitters per turn. Additional parameters: $r_0 = 0.05\lambda_0$, $a = 0.175\lambda_0$.

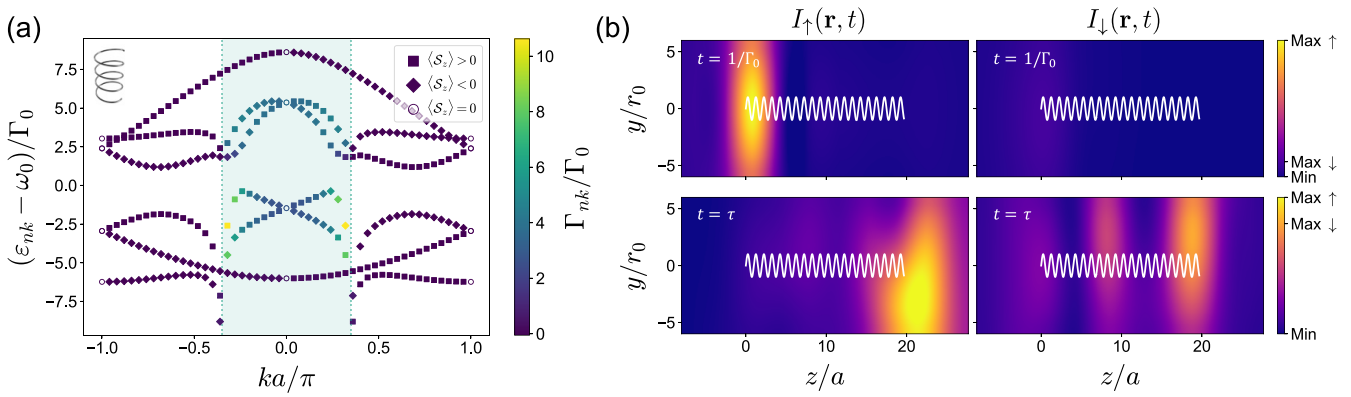

FIG. 4. (a) Collective excitation band structure for an infinite left-handed helix with the same parameters as in Fig. 2. Filled squares (diamonds) denote modes that are predominantly spin ↑ (↓). Open circles indicate equal superposition modes. The coloring of each symbol denotes the collective decay rate of each mode Γ_{nk}. Dotted lines indicate the light cone at $k = k_0$. (b) Snapshots of the emitted electric field intensity $I_\sigma(\mathbf{r}, t)$ at $t = 1/\Gamma_0$ (top two panels) and $t = \tau$ (bottom two panels). The left (right) two panels show the contribution from spin ↑ (↓) photons to the field intensity. Brighter colors demonstrate helical superradiance that is enhanced at either end of the helix. Field intensities are shown in the y-z plane at a distance $x = 10r_0$ from the helical axis so as to not include contributions from the evanescent fields of the emitters. A projection of the helix geometry onto the y-z plane is shown in white. Color bars indicate the relative field intensity of each polarization.

π rotation is also equivalent to a change of initial condition from emitter $i = 1$ to $i = N$ followed by a trivial azimuthal rotation about the z axis.

The dependence of the spin polarization on the helix length and the number of emitters per turn is shown in Fig. 3(b). The $\mathcal{N} = 1$ and $\mathcal{N} = 2$ configurations correspond to the uniform chain and the staggered chain, respectively. These geometries are not chiral and do not exhibit any spin polarization. For the true helices ($\mathcal{N} \geqslant 3$), there is a modest increase in the spin polarization with increasing helix length. This trend has also been reported for spin polarizations of helical electrons in the CISS effect [50] and may be a common feature of helicity-dependent transport.

III. EMERGENT SPIN-ORBIT COUPLING AND HELICAL SUPERRADIANCE

The chirality-dependent dynamics described above can be understood by examining the band structure of the collective helical modes [Fig. 4(a)]. Equation (2) can be expressed in momentum space by performing the discrete Fourier transform $b_{i\sigma} = (1/\sqrt{M}) \sum_{\mathbf{k}} \exp(i\mathbf{k} \cdot \mathbf{r}_m) b_{k\mu\sigma}$, where μ is the sublattice index denoting the M emitters along one sublattice, $\mathbf{r}_m$ is the position of unit cell m, and $\mathbf{k} = k\hat{\mathbf{z}}$ is the lattice quasimomentum (Appendix C). The eigenstates of the resultant k-space Hamiltonian are collective Bloch modes of the form $|\psi_{nk}\rangle = e^{ikz}|u_{nk}\rangle$ with complex eigenvalues $\tilde{\varepsilon}_{nk} = \varepsilon_{nk} + i\Gamma_{nk}$ and band index n. Here, ε_{nk} is the energy of each Bloch mode and Γ_{nk} is the corresponding vacuum decay rate, as indicated by the color coding of symbols in Fig. 4(a). Equation (2) breaks spin rotation symmetry $[H_{\text{eff}}, \mathcal{S}_z] \neq 0$ through the term $\propto b^\dagger_{i,\uparrow} b_{j,\downarrow}$ but is invariant under the combined operation of spatial inversion and spin-flip. Denoting the usual spatial inversion (parity) operator as $\mathcal{P}$, this anti-inversion symmetry can be written as $\bar{\mathcal{P}} = \mathcal{P} \otimes \sigma_x$ and results in antisymmetric spin textures for the Bloch bands. $\bar{\mathcal{P}}$ transforms $(k, \mathcal{S}_z) \to (-k, -\mathcal{S}_z)$ and therefore requires modes with quasimomentum $\pm k$ to have equal energy but opposite spin and group velocity $v = d\varepsilon_k/dk$. Besides the $\bar{\mathcal{P}}$-invariant points at $k = 0, \pm\pi/a$ (at which $\langle \mathcal{S}_z \rangle = 0$), broken spin rotation symmetry allows each mode to experience spin mixing. The spin of each Bloch mode is allowed to be nonzero for arbitrary $k \neq 0, \pm\pi/a$ when the geometry is chiral. This property allows modes with finite dispersion ($v \neq 0$) to experience SOC and results in more efficient transport of spin excitations in the $\chi = -1$ configuration. The nontrivial spin dynamics result from the broken mirror symmetry of the system and are a general feature of arbitrary chiral geometries [51].

The antisymmetric spin textures and associated helicity-dependent chiral transport are protected by $\bar{\mathcal{P}}$ symmetry, irrespective of the presence or absence of dissipation (Appendix D and Fig. 8). Nevertheless, inclusion of the anti-Hermitian term in Eq. (2) enhances this dynamical effect due to collective dissipation at subwavelength scales. In this regime, cooperative resonances can enhance or suppress the decay rate of a given mode away from the bare emitter decay rate Γ_0 depending on whether that mode lies inside or outside the light cone [dotted lines in Fig. 4(a)]. Bright modes (those inside the light cone) are superradiant with $\Gamma_{nk} > \Gamma_0$, whereas dark modes (outside the light cone) experience a momentum mismatch with the available vacuum modes and are subradiant with $\Gamma_{nk} \approx 0$. The dissipative part of Eq. (2) breaks time-reversal symmetry but does not alter the symmetry properties of the spin bands under $\bar{\mathcal{P}}$. Moreover, the decay rates of the Bloch modes may be interpreted as imaginary energies resulting from evolution with H_{eff}. Therefore, as for the real energies, symmetry under $\bar{\mathcal{P}}$ requires that Γ_{nk} be equal for modes with $\pm k$. Because these modes necessarily have opposite spin and group velocity, they also have identical helicity. As such, the two maximally superradiant modes always enhance the population loss for the same photon helicity. Because mirror reflection transforms $\xi \to -\xi$ and $\eta \to -\eta$, the superradiant helicity is reversed between the left- and right-handed chiralities and amplifies the chiral

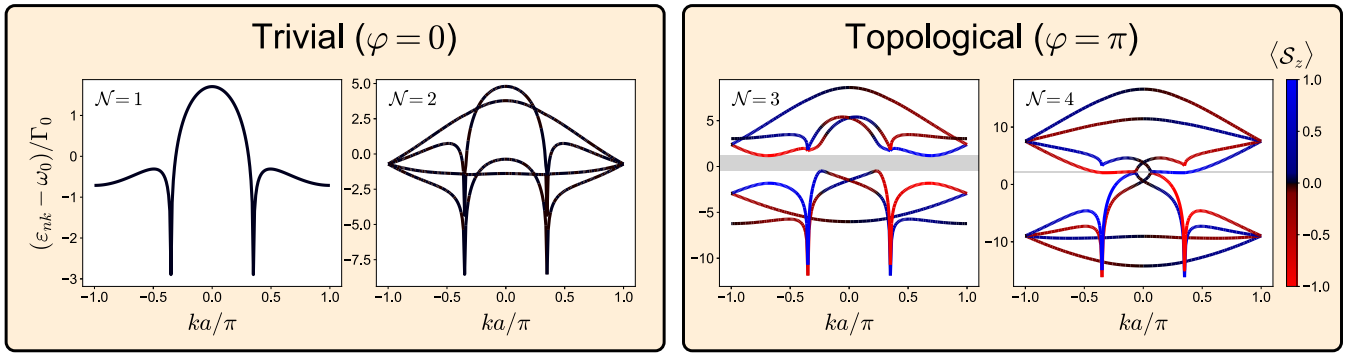

FIG. 5. Demonstration of nontrivial topological properties for chiral geometries. Each plot shows the collective band structure for a left-handed helix constructed with $\mathcal{N}$ emitters per 2π turn. The radius and pitch are the same as in Figs. 2 and 4. Topologically nontrivial band structures occur for $\mathcal{N} \geqslant 3$ and are characterized by the opening of an energy band gap (gray shaded regions) and a nontrivial Zak phase φ. Colors show the spin character $\langle \mathcal{S}_z \rangle$ of each mode and demonstrate the emergence of a finite SOC in the topologically nontrivial regime.

transport. This dynamical effect results in the preferential emission of circularly polarized photons with polarization determined by the propagation direction and chirality of the geometry.

Helicity-dependent superradiant photon emission (helical superradiance) is demonstrated explicitly in Fig. 4(b). For each polarization, the positive frequency electric dipole field at each point $\mathbf{r}$ is given by

$$\mathbf{E}^{+}_{\sigma}(\mathbf{r}) = \sqrt{\frac{6\pi^2\Gamma_0}{\lambda_0\epsilon_0}} \sum_{j=1}^{N} \mathbf{G}(\mathbf{r} - \mathbf{r}_j, \omega_0) \cdot \hat{\varepsilon}_{j\sigma} |g\rangle\langle\sigma_j|, \quad (5)$$

where $|\sigma_j\rangle = b^{\dagger}_{j\sigma}|g\rangle$, $|g\rangle$ is the zero-excitation state and ϵ_0 is the vacuum permittivity (Appendix A). The left (right) panels show the intensity of the emitted field, $I_\sigma(\mathbf{r}, t) = \langle \mathbf{E}^{-}_{\sigma}(\mathbf{r}) \cdot \mathbf{E}^{+}_{\sigma}(\mathbf{r}) \rangle$, radiated by $\uparrow$ ($\downarrow$) excitations. The top two panels show the initial superradiant burst at $t = 1/\Gamma_0$ after initialization with an unpolarized mixed state at the bottom end of the helix [see also top left panel of Fig. 1(d)]. The intense emission of $\uparrow$-polarized photons results from dynamically generated overlaps between the evolving state $\rho(t)$ and the positive helicity superradiant modes of Fig. 4(a). At intermediate times, the wave packet enters subradiant guided modes [30] and radiation into the vacuum via the bulk emitters is suppressed. Strong superradiant emission of $\uparrow$-polarized photons resumes at $t = \tau$ out of the opposite end of the helix [bottom two panels of Fig. 4(b)]. At all times, the maximum radiation intensity of $\downarrow$-polarized photons is strongly suppressed and remains near the minimum radiation intensity for both polarizations. The helix therefore acts as a directional filter for circularly polarized photons.

IV. TOPOLOGICAL PROPERTIES

The SOC identified above implicates a nontrivial topology for the energy bands of chiral geometries [52–55]. Conservation of angular momentum requires that the two-body spin-flip process in Eq. (3) picks up a complex phase $J^{\uparrow\downarrow}_{ij} \propto \exp\{-i(\phi_i + \phi_j)\}$ related to the azimuthal positions of the two emitters ϕ_i and ϕ_j to compensate for the changing photon polarization [see also Fig 1(c)]. This phase dependence, which stems from the electromagnetic Green's tensor (Appendix A), gives rise to an emergent gauge field that results in a nontrivial topology. In 1D, the topological properties of the band structure are characterized by the Zak phase [56],

$$\varphi = \oint_{\mathcal{C}} \mathrm{Tr}[\mathbf{A}(k)] dk, \quad (6)$$

where $A_{mn}(k) = i\langle u_{mk}|\partial_k u_{nk}\rangle$ is the non-Abelian Berry connection [37] and $\mathcal{C}$ defines a closed loop in reciprocal space around the Brillouin zone torus. The Zak phase for an inversion (anti)symmetric unit cell is defined modulo 2π and can be either 0 (trivial) or π (nontrivial).

Figure 5 demonstrates the emergence of nontrivial topological properties as a function of the number of atoms per turn $\mathcal{N}$. When $\mathcal{N} = 1$, the lattice is a simple 1D chain of emitters with lattice spacing a. In this case, the two spin manifolds are uncoupled with $J^{\uparrow\downarrow}_{ij} = 0$, and the band structure consists of two degenerate copies of the band structure for a chain of transversely polarized two-level emitters [30]. Spin rotation symmetry requires that the two degenerate states at each k have $\langle \mathcal{S}_z \rangle = \pm 1$, which averages to zero at every point in the Brillouin zone. For $\mathcal{N} = 2$, the geometry is that of a staggered chain with longitudinal separation a and transverse separation $2r_0$. Here, uniform spin mixing occurs at each mode through $J^{\uparrow\downarrow}_{ij} \neq 0$, and the band structure resembles that of two 1D chains separated by a finite interaction energy. The presence of reflection symmetry for $\mathcal{N} = 1, 2$ prohibits the emergence of a finite SOC. The minimal chiral geometry is realized for $\mathcal{N} = 3$, resulting in a finite energy gap and SO coupled bands. The Zak phases calculated on either side of the energy gap are nontrivial, indicating a topologically nontrivial band structure. This nontrivial topology persists for $\mathcal{N} \geqslant 3$ as long as the geometry remains chiral.

V. TOWARDS EXPERIMENTAL REALIZATIONS

Our results describe helicity-dependent superradiant photon emission that occurs in chiral systems of dipole-coupled emitters. This formalism naturally includes neutral atom-based platforms that are being investigated for use in emerging quantum technologies. Our findings also introduce an exciting avenue for cold atom quantum simulators, which could be used to study the governing properties of chirality-dependent

transport (including the CISS effect) in a well-controlled environment. Such simulators could also be used to investigate the influence of helical superradiance on the excitation lifetimes of chiral molecules. The exploration of such processes at the single-atom scale could have far-reaching implications for both technological and biological applications [57], and should be experimentally observable with readily available techniques.

A standard approach would be to realize the helical geometry using neutral atoms in a 3D optical tweezer array. Coherent oscillations between atoms with V-type level structures have been demonstrated, e.g., by isolating the $60S_{1/2}$ and $60P_{3/2}$ Rydberg manifolds of ^{87}Rb [58,59]. The 17.2 GHz transition frequency between these manifolds allows for subwavelength dynamics at μm-scale tweezer separations. Although the influence of dissipation may not be observable with this platform due to long Rydberg excitation lifetimes, the chirality dependent transport and topological properties of the system could still be achieved.

Dissipative dynamics could, however, be observed in a similar setup using the $^3P_0$ and $^3D_1$ manifolds of ^{88}Sr [24], which is commonly used in 3D optical lattice clocks [60]. Helical arrangements of atoms could be built by selectively loading particular sites of the optical lattice using an extension of the tweezer-based programmable loading scheme recently demonstrated for 2D optical lattices [61] or by employing holographic optical traps made from dielectric metasurfaces [62]. Techniques for measuring topological Bloch bands simulated with optical lattices are well-established [55,63,64].

An alternative setup based on a Laguerre-Gauss mode optical trapping potential may also be realized with readily available techniques [65–67]. Laguerre-Gauss modes are eigenmodes of the paraxial wave equation with orbital angular momentum quantum number l. The $l = 1$ mode exhibits a cylindrical geometry with a phase advance that winds once per wavelength. Interfering this mode with an orthogonally polarized plane wave shapes the field intensity into a helix. Intersecting this field with a cloud of red-detuned atoms would trap some of these atoms at intensity maxima determined by the helical potential. An additional long-range interaction potential (which could be imposed by Rydberg dressing the atoms via an additional laser [68,69]) would result in a periodic arrangement of atoms along the helix.

VI. OUTLOOK

Here we have demonstrated the helicity-dependent transport and superradiant emission of circularly polarized photons from chiral arrangements of atoms or molecules. This phenomenon has a complete description within the electric dipole approximation, placing it within the class of nonmagnetic chiral interactions exhibiting very strong optical responses [70,71]. Precise control over the transport and emission of photons is a fundamental goal of quantum information science and could contribute to the development of new quantum technologies. Our findings also represent an exciting opportunity for cold atom quantum simulators towards studying chirality dependent transport and chiral light-matter interactions at the single-atom scale.

Our results also shed light on the governing principles of spin selective electron transport in the CISS effect. Presently, there is no consensus explanation for the extremely large spin polarizations produced by carbon-based molecules with weak intrinsic SO interactions. Here, however, we have demonstrated extremely large spin polarizations based on geometrical considerations alone. A chirality-induced gauge field like that in Eq. (6) has, to our knowledge, not been considered in any theoretical analysis of CISS thus far, and may be important in explaining the robustness of the effect at room temperature. The very significant influence of helical superradiance further suggests that dissipation is crucial for achieving strong helicity-dependent transport. For the results described in this paper, the preferential scattering of excitations with the "wrong" helicity greatly enhances the observed spin polarization as compared to the fully Hermitian case (Appendix D and Fig. 8). Accounting for topologically protected spin polarizations and the influence of dissipation might resolve the discrepancies between theoretical and experimental models of CISS.

As has been suggested for the electron spin, these chirality-dependent phenomena might also play a role in chemical or biological processes in nature. The large optical response associated with helical superradiance could allow for additional types of chiral-selective photochemistry driven by circularly polarized light, without reliance on higher order multipole moments. In particular, the well-documented importance of photoexcitation dynamics to the stability and reactivity of (pre)biotic molecules (e.g., RNA, DNA) [72–74] evokes the question of whether such a process might have contributed to the emergence of biological homochirality. Although the mechanisms responsible for the homochirality of life are unknown, recent studies have suggested that chiral selective processes during prebiotic synthesis could have seeded an initial imbalance that was amplified by subsequent chemical reactions [75,76]. In particular, a bias in the net flux of circularly polarized photons—as has been observed in nearby star forming regions [77–79]—has long been suggested as a potential symmetry breaking agent [80–82]. However, previous attempts to translate this bias into homochiral chemistry using traditional (magnetic) chiroptical phenomena typically result in asymmetries of only a few percent [83–86]. The helical superradiance identified in this paper provides another mechanism for chiral amplification that does not rely on weak magnetic interactions and could potentially lead to a much larger chiral bias.

ACKNOWLEDGMENTS

The authors thank M. D. Lukin and J. Simon for discussions on quantum simulators, D. D. Sasselov and R. Szabla for discussions on chiral molecules, and C. B. Dag for discussions on topological band theory. S.O. is supported by a postdoctoral fellowship of the Max Planck-Harvard Research Center for Quantum Optics. All authors acknowledge funding from the National Science Foundation (NSF) via the Center for Ultracold Atoms (CUA) Physics Frontiers Centers (PFC) program and via PHY-2207972, as well as from the Air Force Office of Scientific Research (AFOSR).

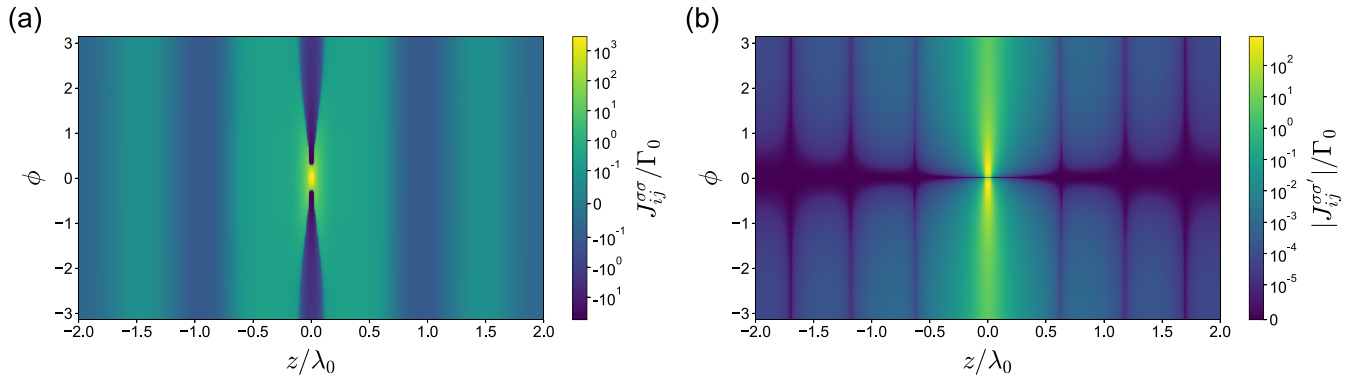

FIG. 6. Coherent coupling strengths between atoms i and j located on a helix with radius $r_0 = 0.05\lambda_0$. The x axis denotes the relative distance between the emitters in the $\hat{\mathbf{z}}$ direction (along the longitudinal helical axis). The y axis denotes the relative azimuthal coordinate between the emitters. (a) Spin-preserving interactions. Colors denote the interaction strength $J_{ij}^{\sigma\sigma}/\Gamma_0$ with $\sigma \in \{\uparrow, \downarrow\}$. (b) Spin-flipping interactions. Colors denote the interaction strength $|J_{ij}^{\sigma\sigma'}|/\Gamma_0$ with $\sigma, \sigma' \in \{\uparrow, \downarrow\}$ for $\sigma \neq \sigma'$.

APPENDIX A: DIPOLE-DIPOLE INTERACTIONS

The effective dipole-dipole interactions considered in the main text can be derived either by tracing over the field degrees of freedom in a fully second quantized treatment and applying the Born and Markov approximations or by substitution in analogy with classical electrodynamics. Here we present a brief outline of the latter approach and defer the details to the many well-cited references (e.g., Refs. [22,23,30,47–49]). In Lorenz gauge, the classical scalar and vector potentials $\varphi(\mathbf{r}, t)$ and $\mathbf{A}(\mathbf{r}, t)$ obey the inhomogeneous wave equations

$$\nabla^2\varphi - \frac{1}{c}\frac{\partial^2\varphi}{\partial t^2} = -\frac{\varrho}{\epsilon_0}, \tag{A1}$$

$$\nabla^2\mathbf{A} - \frac{1}{c}\frac{\partial^2\mathbf{A}}{\partial t^2} = -\mu_0\mathbf{j}, \tag{A2}$$

where $\varrho(\mathbf{r}, t)$ and $\mathbf{j}(\mathbf{r}, t)$ are the source charge and current densities, c is the speed of light in vacuum, and μ_0 is the vacuum permeability. The general solutions at time t are given in terms of the retarded time $t' = t - |\mathbf{r} - \mathbf{r}'|/c$ for source coordinate $\mathbf{r}'$ as [87]

$$\varphi(\mathbf{r}, t) = \frac{1}{4\pi\epsilon_0}\int d^3r' \frac{\varrho(\mathbf{r}', t')}{|\mathbf{r} - \mathbf{r}'|}, \tag{A3}$$

$$\mathbf{A}(\mathbf{r}, t) = \frac{\mu_0}{4\pi}\int d^3r' \frac{\mathbf{j}(\mathbf{r}', t')}{|\mathbf{r} - \mathbf{r}'|}. \tag{A4}$$

For a time-dependent point electric dipole located at $\mathbf{r}' = 0$ with dipole moment $\mathbf{p}(t')$, the charge density $\varrho(\mathbf{r}, t') = -\mathbf{p}(t')\nabla\delta(\mathbf{r})$ obeys the continuity equation $\nabla\cdot\mathbf{j} = -\partial\varrho/\partial t$, yielding the current density $\mathbf{j}(\mathbf{r}, t') = \delta(\mathbf{r})\dot{\mathbf{p}}(t')$, where $\dot{\mathbf{p}}(t') = (d/dt)\mathbf{p}(t - |r|/c)$. The classical potentials are then given by

$$\varphi(\mathbf{r}, t) = \frac{1}{4\pi\epsilon_0}\left[\frac{\dot{\mathbf{p}}(t')\cdot\mathbf{r}}{c|\mathbf{r}|^2} + \frac{\mathbf{p}(t')\cdot\mathbf{r}}{|\mathbf{r}|^3}\right], \tag{A5}$$

$$\mathbf{A}(\mathbf{r}, t) = \frac{\mu_0}{4\pi}\frac{\dot{\mathbf{p}}(t')}{|\mathbf{r}|}. \tag{A6}$$

For a time-harmonic source oscillating at frequency ω_0, we can write $\mathbf{p}(t) = \wp e^{-i\omega_0 t}$, where the strength and orientation of the dipole are encoded into $\wp$. Using the relations $\mathbf{E} = -\nabla\varphi - \partial\mathbf{A}/\partial t$ and $\omega_0 = ck_0$ for wave number $k_0 = 2\pi/\lambda_0$, the corresponding electric field can be written as $\mathbf{E}(\mathbf{r}, t) = \mathbf{E}(\mathbf{r})e^{-i\omega_0 t}$ with

$$\mathbf{E}(\mathbf{r}) = \mu_0\omega_0^2\frac{e^{ik_0|\mathbf{r}|}}{4\pi k_0^2|\mathbf{r}|^3}\left[\left(k_0^2|\mathbf{r}|^2 + ik_0|\mathbf{r}| - 1\right)\wp - \left(k_0^2|\mathbf{r}|^2 + 3ik_0|\mathbf{r}| - 3\right)(\hat{\mathbf{r}}\cdot\wp)\hat{\mathbf{r}}\right] \tag{A7}$$

and $\hat{\mathbf{r}} = \mathbf{r}/|\mathbf{r}|$. We now treat the dipole as a (Hermitian) quantum operator describing the transition from the ground state $|g\rangle$ to orbital $|\sigma\rangle$. In this case, $\mathbf{p}_\sigma(t) = \wp_\sigma e^{-i\omega_0 t}|g\rangle\langle\sigma| + \wp_\sigma^* e^{i\omega_0 t}|\sigma\rangle\langle g|$, and the resulting electric field becomes $\mathbf{E}_\sigma(\mathbf{r}) = \mathbf{E}_\sigma^+(\mathbf{r}) + \mathbf{E}_\sigma^-(\mathbf{r})$, where

$$\mathbf{E}_\sigma^+(\mathbf{r}) = \mu_0\omega_0^2\mathbf{G}(\mathbf{r}, \omega_0)\cdot\wp_\sigma|g\rangle\langle\sigma|, \tag{A8}$$

$\mathbf{E}_\sigma^-(\mathbf{r}) = (\mathbf{E}_\sigma^+(\mathbf{r}))^\dagger$, and we have defined the free-space electromagnetic Green's tensor

$$\mathbf{G}(\mathbf{r}, \omega_0) = \frac{e^{ik_0|\mathbf{r}|}}{4\pi k_0^2|\mathbf{r}|^3}\left[\left(k_0^2|\mathbf{r}|^2 + ik_0|\mathbf{r}| - 1\right)\mathbb{1} - \left(k_0^2|\mathbf{r}|^2 + 3ik_0|\mathbf{r}| - 3\right)\frac{\mathbf{r}\otimes\mathbf{r}}{|\mathbf{r}|^2}\right]. \tag{A9}$$

Defining the spontaneous emission rate $\Gamma_0 = \omega_0^3|\wp|_\sigma^2/(3\pi\hbar\epsilon_0 c^3)$ for $\wp_\sigma = |\wp_\sigma|\hat{\varepsilon}_\sigma$ and substituting the relation $c^2 = 1/(\epsilon_0\mu_0)$ yields Eq. (5) of the main text. Finally, the interemitter couplings of Eq. (3) follow from the dipole-dipole interaction $-\mathbf{p}_{i\sigma}\cdot\mathbf{E}_{j\sigma}$ after applying the rotating wave approximation and tracing over the ground state. The coherent spin-preserving and spin-flipping interactions are shown for the helical geometry in Fig. 6.

APPENDIX B: CHIRAL PHOTOEXCITATION BIAS FROM CIRCULARLY POLARIZED LIGHT

The results of the main text are presented based on an initially unpolarized statistical mixture of right and left circularly polarized excitations. In this case, the preferential excitation of a given spin manifold depends on the chirality of the helix and on the propagation direction of the initial wave packet

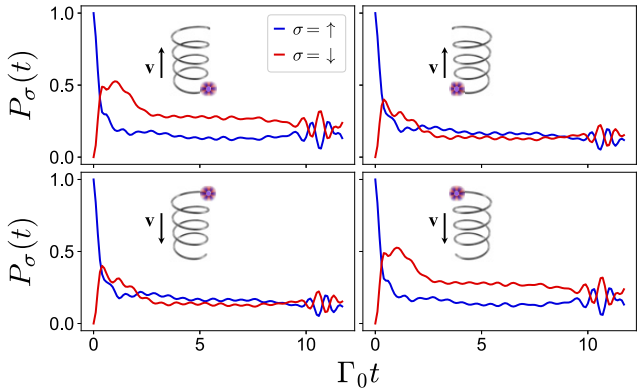

FIG. 7. Preferential excitation of one chirality from an unequally polarized initial state. Panels correspond to the same setups as in Fig. 2(a) of the main text but for initial states $\rho(0) = |\uparrow_i\rangle\langle\uparrow_i|$, corresponding to a polarized spin up excitation localized at the bottom (top two panels) or top (bottom two panels) of the helix.

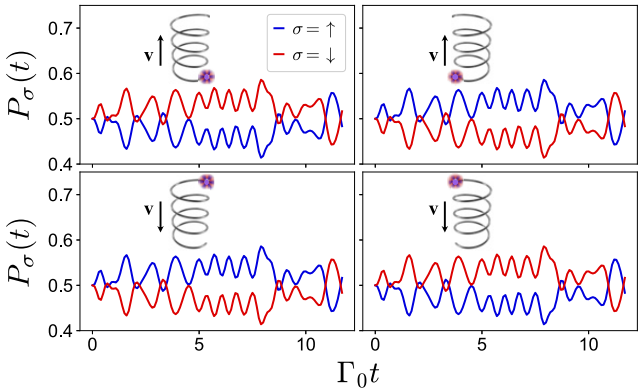

FIG. 8. Helicity-dependent chiral transport without dissipation. Panels correspond to the same setups as in Fig. 2(a) of the main text but without the influence of the anti-Hermitian term in Eq. (2) [i.e., time evolution with only the Hamiltonian (1)].

relative to the quantization axis. Here we demonstrate that the initial excitation of only a single spin orbital (e.g., by the absorption of pure circularly polarized light) results in the long-lived excitation of only one chirality. Figure 3 shows the transport dynamics for the initial state $\rho(0) = |\uparrow_i\rangle\langle\uparrow_i|$, corresponding to a polarized spin-up excitation localized at the bottom (top two panels) or top (bottom two panels) of the helix. For a given propagation direction, one chirality is excited into long-lived subradiant modes while the other decays rapidly via helical superradiance. If such a process were to occur inside right- and left-handed chiral molecules, the discrepancy in photoexcitation lifetimes could lead to differences in chiral photochemistry.

APPENDIX C: BAND STRUCTURE CALCULATIONS

For the case of an infinite helix, we can describe the geometry as a non-Bravais lattice composed of $\mathcal{N}$ sublattices. Decomposing the site index i into a unit cell index m and a sublattice index μ, we make the discrete Fourier transform $b_{m\mu\sigma} = (1/\sqrt{M})\sum_{\mathbf{k}} \exp(i\mathbf{k}\cdot\mathbf{r}_m) b_{k\mu\sigma}$, where $\mathbf{k}$ is the lattice quasimomentum. This transformation yields $H_{\text{eff}} = \sum_{\mathbf{k}} H(\mathbf{k})$, where the Bloch Hamiltonian is given by

$$H(\mathbf{k}) = \sum_{\mu,\nu}\sum_{\sigma,\sigma'} h_{\mu\sigma,\nu\sigma'}(\mathbf{k}) b^\dagger_{\mathbf{k}\mu\sigma} b_{\mathbf{k}\nu\sigma'}. \tag{C1}$$

Here, the matrix elements

$$h_{\mu\sigma,\nu\sigma'}(\mathbf{k}) = \omega_0 \delta_{\mu\nu}\delta_{\sigma\sigma'} + \chi^I_{\mu\sigma,\nu\sigma'} + \chi^{II}_{\mu\sigma,\nu\sigma'} \tag{C2}$$

can be written in terms of infinite sums over the set of Bravais lattice vectors $\mathbf{R}_\mu$ as [51,88,89]

$$\chi^I_{\mu\sigma,\nu\sigma'} = -\frac{3}{2}\lambda_0\Gamma_0 \sum_{\mathbf{R}_\mu \neq 0} e^{-i\mathbf{k}\cdot\mathbf{R}_\mu} G_{\sigma\sigma'}(\mathbf{R}_\mu)\delta_{\mu\nu}, \tag{C3}$$

$$\chi^{II}_{\mu\sigma,\nu\sigma'} = -\frac{3}{2}\lambda_0\Gamma_0 \sum_{\mathbf{R}_\mu} e^{-i\mathbf{k}\cdot\mathbf{R}_\mu} G_{\sigma\sigma'}(\mathbf{R}_\mu + \mathbf{n}_{\mu\nu})(1-\delta_{\mu\nu}), \tag{C4}$$

where the basis vectors $\mathbf{n}_{\mu\nu} = \mathbf{n}_\mu - \mathbf{n}_\nu$ point from sublattice ν to μ within a given unit cell and $G_{\sigma\sigma'}(\mathbf{R}_\mu) = \hat{\varepsilon}^\dagger_\sigma \cdot \mathbf{G}(\mathbf{R}_\mu)\cdot\hat{\varepsilon}_{\sigma'}$. To solve for the band structures presented in Figs. 4(a) and 5, we discretize the Brillouin zone as $\mathbf{k} = k\hat{\mathbf{k}}$ for $k = \pi j/(Ma)$. Here, $a = |\mathbf{r}_{m+1} - \mathbf{r}_m|$ is the lattice spacing between adjacent unit cells and $j = 0, ..., 2M$ is an integer. The band structures are then obtained by numerically diagonalizing the Bloch Hamiltonian for each k.

APPENDIX D: CHIRALITY DEPENDENT PHOTON TRANSPORT WITHOUT DISSIPATION

As discussed in the main text, the preferential transport of excitations with a given helicity stems from an emergent SOC induced by the chiral geometry. This SOC results in antisymmetric spin textures for the Bloch bands and is protected by $\bar{\mathcal{P}}$ symmetry. Helical superradiance enhances this effect through dissipation, but is not necessary for chirality dependent transport. Figure 8 shows the population dynamics in the absence of dissipation. The unitary dynamics generated by the Hermitian Hamiltonian (1) are sufficient to produce the helical transport.

[1] K. Ray, S. P. Ananthavel, D. H. Waldeck, and R. Naaman, Asymmetric scattering of polarized electrons by organized organic films of chiral molecules, Science **283**, 814 (1999).

[2] B. Göhler, V. Hamelbeck, T. Z. Markus, M. Kettner, G. F. Hanne, Z. Vager, R. Naaman, and H. Zacharias, Spin selectivity in electron transmission through self-assembled monolayers of double-stranded DNA, Science **331**, 894 (2011).

[3] I. Žutić, J. Fabian, and S. Das Sarma, Spintronics: Fundamentals and applications, Rev. Mod. Phys. **76**, 323 (2004).

[4] R. Naaman and D. H. Waldeck, Spintronics and chirality: Spin selectivity in electron transport through chiral molecules, Annu. Rev. Phys. Chem. **66**, 263 (2015).

[5] K. Michaeli, V. Varade, R. Naaman, and D. H. Waldeck, A new approach towards spintronics–spintronics with

no magnets, J. Phys.: Condens. Matter **29**, 103002 (2017).

[6] O. Ben Dor, S. Yochelis, A. Radko, K. Vankayala, E. Capua, A. Capua, S.-H. Yang, L. T. Baczewski, S. S. P. Parkin, R. Naaman, and Y. Paltiel, Magnetization switching in ferromagnets by adsorbed chiral molecules without current or external magnetic field, Nat. Commun. **8**, 14567 (2017).

[7] K. Kondou, M. Shiga, S. Sakamoto, H. Inuzuka, A. Nihonyanagi, F. Araoka, M. Kobayashi, S. Miwa, D. Miyajima, and Y. Otani, Chirality-induced magnetoresistance due to thermally driven spin polarization, J. Am. Chem. Soc. **144**, 7302 (2022).

[8] R. Naaman, D. H. Waldeck, and Y. Paltiel, Chiral molecules-ferromagnetic interfaces, an approach towards spin controlled interactions, Appl. Phys. Lett. **115**, 133701 (2019).

[9] S.-H. Yang, R. Naaman, Y. Paltiel, and S. S. P. Parkin, Chiral spintronics, Nat. Rev. Phys. **3**, 328 (2021).

[10] R. Nakajima, D. Hirobe, G. Kawaguchi, Y. Nabei, T. Sato, T. Narushima, H. Okamoto, and H. M. Yamamoto, Giant spin polarization and a pair of antiparallel spins in a chiral superconductor, Nature (London) **613**, 479 (2023).

[11] Y. Adhikari, T. Liu, H. Wang, Z. Hua, H. Liu, E. Lochner, P. Schlottmann, B. Yan, J. Zhao, and P. Xiong, Interplay of structural chirality, electron spin and topological orbital in chiral molecular spin valves, Nat. Commun. **14**, 5163 (2023).

[12] K. Kim, E. Vetter, L. Yan, C. Yang, Z. Wang, R. Sun, Y. Yang, A. H. Comstock, X. Li, J. Zhou, L. Zhang, W. You, D. Sun, and J. Liu, Chiral-phonon-activated spin Seebeck effect, Nat. Mater. **22**, 322 (2023).

[13] R. Naaman, Y. Paltiel, and D. H. Waldeck, Chiral induced spin selectivity gives a new twist on spin-control in chemistry, Acc. Chem. Res. **53**, 2659 (2020).

[14] J. M. Abendroth, D. M. Stemer, B. P. Bloom, P. Roy, R. Naaman, D. H. Waldeck, P. S. Weiss, and P. C. Mondal, Spin selectivity in photoinduced charge-transfer mediated by chiral molecules, ACS Nano **13**, 4928 (2019).

[15] I. Carmeli, K. S. Kumar, O. Heifler, C. Carmeli, and R. Naaman, Spin selectivity in electron transfer in photosystem I, Angew. Chem. Int. Ed. **53**, 8953 (2014).

[16] K. Michaeli, N. Kantor-Uriel, R. Naaman, and D. H. Waldeck, The electron's spin and molecular chirality – how are they related and how do they affect life processes? Chem. Soc. Rev. **45**, 6478 (2016).

[17] S. F. Ozturk and D. D. Sasselov, On the origins of life's homochirality: Inducing enantiomeric excess with spin-polarized electrons, Proc. Natl. Acad. Sci. USA **119**, e2204765119 (2022).

[18] K. Y. Bliokh, F. J. Rodríguez-Fortuño, F. Nori, and A. V. Zayats, Spin–orbit interactions of light, Nat. Photon. **9**, 796 (2015).

[19] K. Y. Bliokh and F. Nori, Transverse and longitudinal angular momenta of light, Phys. Rep. **592**, 1 (2015).

[20] K. Y. Bliokh, A. Y. Bekshaev, and F. Nori, Optical momentum, spin, and angular momentum in dispersive media, Phys. Rev. Lett. **119**, 073901 (2017).

[21] P. Lodahl, S. Mahmoodian, S. Stobbe, A. Rauschenbeutel, P. Schneeweiss, J. Volz, H. Pichler, and P. Zoller, Chiral quantum optics, Nature (London) **541**, 473 (2017).

[22] R. H. Lehmberg, Radiation from an *N*-atom system. I. General formalism, Phys. Rev. A **2**, 883 (1970).

[23] R. H. Lehmberg, Radiation from an *N*-atom system. II. Spontaneous emission from a pair of atoms, Phys. Rev. A **2**, 889 (1970).

[24] B. Olmos, D. Yu, Y. Singh, F. Schreck, K. Bongs, and I. Lesanovsky, Long-range interacting many-body systems with alkaline-Earth-m atoms, Phys. Rev. Lett. **110**, 143602 (2013).

[25] R. Gutiérrez-Jáuregui and A. Asenjo-Garcia, Directional transport along an atomic chain, Phys. Rev. A **105**, 043703 (2022).

[26] S. J. Jang and B. Mennucci, Delocalized excitons in natural light-harvesting complexes, Rev. Mod. Phys. **90**, 035003 (2018).

[27] R. Holzinger, J. S. Peter, S. Ostermann, H. Ritsch, and S. Yelin, Harnessing quantum emitter rings for efficient energy transport and trapping, Opt. Quantum **2**, 57 (2024).

[28] R. H. Dicke, Coherence in spontaneous radiation processes, Phys. Rev. **93**, 99 (1954).

[29] M. Gross and S. Haroche, Superradiance: An essay on the theory of collective spontaneous emission, Phys. Rep. **93**, 301 (1982).

[30] A. Asenjo-Garcia, M. Moreno-Cardoner, A. Albrecht, H. J. Kimble, and D. E. Chang, Exponential improvement in photon storage fidelities using subradiance and "selective radiance" in atomic arrays, Phys. Rev. X **7**, 031024 (2017).

[31] M. Reitz, C. Sommer, and C. Genes, Cooperative quantum phenomena in light-matter platforms, PRX Quantum **3**, 010201 (2022).

[32] M. Barbatti, Simulation of excitation by sunlight in mixed quantum-classical dynamics, J. Chem. Theory Comput. **16**, 4849 (2020).

[33] C. L. Kufner, S. Crucilla, D. Ding, P. Stadlbauer, J. Šponer, J. W. Szostak, D. D. Sasselov, and R. Szabla, Photoinduced charge separation and DNA self-repair depend on sequence directionality and stacking pattern, Chem. Sci. **15**, 2158 (2024).

[34] C. L. Kufner, D. B. Bucher, and D. D. Sasselov, The photophysics of nucleic acids: Consequences for the emergence of life, ChemSystemsChem **5**, e202200019 (2023).

[35] C. L. Kufner, W. Zinth, and D. B. Bucher, UV-induced charge-transfer states in short guanosine-containing DNA oligonucleotides, ChemBioChem **21**, 2306 (2020).

[36] Z. R. Todd, R. Szabla, J. W. Szostak, and D. D. Sasselov, UV photostability of three 2-aminoazoles with key roles in prebiotic chemistry on the early earth, Chem. Commun. **55**, 10388 (2019).

[37] F. Wilczek and A. Zee, Appearance of gauge structure in simple dynamical systems, Phys. Rev. Lett. **52**, 2111 (1984).

[38] K. Y. Bliokh, D. Smirnova, and F. Nori, Quantum spin Hall effect of light, Science **348**, 1448 (2015).

[39] M. Segev and M. A. Bandres, Topological photonics: Where do we go from here? Nanophotonics **10**, 425 (2020).

[40] T. Ozawa, H. M. Price, A. Amo, N. Goldman, M. Hafezi, L. Lu, M. C. Rechtsman, D. Schuster, J. Simon, O. Zilberberg, and I. Carusotto, Topological photonics, Rev. Mod. Phys. **91**, 015006 (2019).

[41] M. Hafezi, E. A. Demler, M. D. Lukin, and J. M. Taylor, Robust optical delay lines with topological protection, Nat. Phys. **7**, 907 (2011).

[42] S. V. Syzranov, M. L. Wall, V. Gurarie, and A. M. Rey, Spin–orbital dynamics in a system of polar molecules, Nat. Commun. **5**, 5391 (2014).

[43] R. Y. Chiao and Y.-S. Wu, Manifestations of Berry's topological phase for the photon, Phys. Rev. Lett. **57**, 933 (1986).

[44] Z. Wang, Y. Chong, J. D. Joannopoulos, and M. Soljačić, Observation of unidirectional backscattering-immune topological electromagnetic states, Nature (London) **461**, 772 (2009).

[45] D. MacDonald, K. Herbert, X. Zhang, T. Polgruto, and P. Lu, Solution structure of an A-tract DNA bend, J. Mol. Biol. **306**, 1081 (2001).

[46] V. May and O. Kühn, *Charge and Energy Transfer Dynamics in Molecular Systems*, 1st ed. (Wiley, Weinheim, Germany, 2011).

[47] H.-P. Breuer and F. Petruccione, *The Theory of Open Quantum Systems* (Oxford University Press, Oxford, 2002).

[48] M. O. Scully and M. S. Zubairy, *Quantum Optics*, 6th ed. (Cambridge University Press, Cambridge, 2008).

[49] A. Asenjo-Garcia, J. D. Hood, D. E. Chang, and H. J. Kimble, Atom-light interactions in quasi-one-dimensional nanostructures: A Green's-function perspective, Phys. Rev. A **95**, 033818 (2017).

[50] S. Mishra, A. K. Mondal, S. Pal, T. K. Das, E. Z. B. Smolinsky, G. Siligardi, and R. Naaman, Length-dependent electron spin polarization in oligopeptides and DNA, J. Phys. Chem. C **124**, 10776 (2020).

[51] J. S. Peter, S. Ostermann, and S. F. Yelin, Chirality-induced emergent spin-orbit coupling in topological atomic lattices, arXiv:2311.09303.

[52] C. Kane, Topological band theory and the Z_2 invariant, in *Contemporary Concepts of Condensed Matter Science* (Elsevier, Amsterdam, The Netherlands, 2013), Vol. 6, pp. 3–34.

[53] B. I. Halperin, Quantized Hall conductance, current-carrying edge states, and the existence of extended states in a two-dimensional disordered potential, Phys. Rev. B **25**, 2185 (1982).

[54] C. L. Kane and E. J. Mele, Quantum spin Hall effect in graphene, Phys. Rev. Lett. **95**, 226801 (2005).

[55] M. Atala, M. Aidelsburger, J. T. Barreiro, D. Abanin, T. Kitagawa, E. Demler, and I. Bloch, Direct measurement of the Zak phase in topological Bloch bands, Nat. Phys. **9**, 795 (2013).

[56] J. Zak, Berry's phase for energy bands in solids, Phys. Rev. Lett. **62**, 2747 (1989).

[57] P. J. Ollitrault, A. Kandala, C.-F. Chen, P. K. Barkoutsos, A. Mezzacapo, M. Pistoia, S. Sheldon, S. Woerner, J. M. Gambetta, and I. Tavernelli, Quantum equation of motion for computing molecular excitation energies on a noisy quantum processor, Phys. Rev. Res. **2**, 043140 (2020).

[58] S. de Léséleuc, V. Lienhard, P. Scholl, D. Barredo, S. Weber, N. Lang, H. P. Büchler, T. Lahaye, and A. Browaeys, Observation of a symmetry-protected topological phase of interacting bosons with Rydberg atoms, Science **365**, 775 (2019).

[59] V. Lienhard, P. Scholl, S. Weber, D. Barredo, S. de Léséleuc, R. Bai, N. Lang, M. Fleischhauer, H. P. Büchler, T. Lahaye, and A. Browaeys, Realization of a density-dependent Peierls phase in a synthetic, spin-orbit coupled Rydberg system, Phys. Rev. X **10**, 021031 (2020).

[60] S. L. Campbell, R. B. Hutson, G. E. Marti, A. Goban, N. D. Oppong, R. L. McNally, L. Sonderhouse, J. M. Robinson, W. Zhang, B. J. Bloom, and J. Ye, A fermi-degenerate three-dimensional optical lattice clock, Science **358**, 90 (2017).

[61] A. W. Young, W. J. Eckner, N. Schine, A. M. Childs, and A. M. Kaufman, Tweezer-programmable 2D quantum walks in a Hubbard-regime lattice, Science **377**, 885 (2022).

[62] X. Huang, W. Yuan, A. Holman, M. Kwon, S. J. Masson, R. Gutierrez-Jauregui, A. Asenjo-Garcia, S. Will, and N. Yu, Metasurface holographic optical traps for ultracold atoms, Prog. Quantum Electron. **89**, 100470 (2023).

[63] D. A. Abanin, T. Kitagawa, I. Bloch, and E. Demler, Interferometric approach to measuring band topology in 2D optical lattices, Phys. Rev. Lett. **110**, 165304 (2013).

[64] T. Li, L. Duca, M. Reitter, F. Grusdt, E. Demler, M. Endres, M. Schleier-Smith, I. Bloch, and U. Schneider, Bloch state tomography using Wilson lines, Science **352**, 1094 (2016).

[65] L. W. Clark, N. Schine, C. Baum, N. Jia, and J. Simon, Observation of Laughlin states made of light, Nature (London) **582**, 41 (2020).

[66] N. Schine, M. Chalupnik, T. Can, A. Gromov, and J. Simon, Electromagnetic and gravitational responses of photonic Landau levels, Nature (London) **565**, 173 (2019).

[67] N. Schine, A. Ryou, A. Gromov, A. Sommer, and J. Simon, Synthetic Landau levels for photons, Nature (London) **534**, 671 (2016).

[68] J. E. Johnson and S. L. Rolston, Interactions between Rydberg-dressed atoms, Phys. Rev. A **82**, 033412 (2010).

[69] J. Honer, H. Weimer, T. Pfau, and H. P. Büchler, Collective many-body interaction in Rydberg dressed atoms, Phys. Rev. Lett. **105**, 160404 (2010).

[70] D. Ayuso, A. F. Ordonez, and O. Smirnova, Ultrafast chirality: The road to efficient chiral measurements, Phys. Chem. Chem. Phys. **24**, 26962 (2022).

[71] A. F. Ordonez and O. Smirnova, Generalized perspective on chiral measurements without magnetic interactions, Phys. Rev. A **98**, 063428 (2018).

[72] L. M. Nielsen, S. V. Hoffmann, and S. B. Nielsen, Probing electronic coupling between adenine bases in RNA strands from synchrotron radiation circular dichroism experiments, Chem. Commun. **48**, 10425 (2012).

[73] L. M. Nielsen, S. V. Hoffmann, and S. B. Nielsen, Electronic coupling between photo-excited stacked bases in DNA and RNA strands with emphasis on the bright states initially populated, Photochem. Photobiolog. Sci. **12**, 1273 (2013).

[74] I. Buchvarov, Q. Wang, M. Raytchev, A. Trifonov, and T. Fiebig, Electronic energy delocalization and dissipation in single- and double-stranded DNA, Proc. Natl. Acad. Sci. USA **104**, 4794 (2007).

[75] D. G. Blackmond, The origin of biological homochirality, Cold Spring Harbor Perspect. Biol. **2**, a002147 (2010).

[76] J. E. Hein and D. G. Blackmond, On the origin of single chirality of amino acids and sugars in biogenesis, Acc. Chem. Res. **45**, 2045 (2012).

[77] J. Bailey, A. Chrysostomou, J. H. Hough, T. M. Gledhill, A. McCall, S. Clark, F. Ménard, and M. Tamura, Circular polarization in star- formation regions: Implications for biomolecular homochirality, Science **281**, 672 (1998).

[78] T. Fukue, M. Tamura, R. Kandori, N. Kusakabe, J. H. Hough, J. Bailey, D. C. B. Whittet, P. W. Lucas, Y. Nakajima, and J. Hashimoto, Extended high circular polarization in the orion massive star forming region: Implications for the origin of homochirality in the solar system, Origins Life Evol. Biosphere **40**, 335 (2010).

[79] J. Kwon, M. Tamura, P. W. Lucas, J. Hashimoto, N. Kusakabe, R. Kandori, Y. Nakajima, T. Nagayama, T. Nagata, and J. H. Hough, Near-infrared circular polarization images of NGC 6334-V, Astrophys. J. **765**, L6 (2013).

[80] R. Hadidi, D. K. Bozanic, G. A. Garcia, and L. Nahon, Electron asymmetries in the photoionization of chiral molecules: possible astrophysical implications, Adv. Phys.: X **3**, 1477530 (2018).

[81] A. D. Garcia, C. Meinert, H. Sugahara, N. C. Jones, S. V. Hoffmann, and U. J. Meierhenrich, The astrophysical formation of asymmetric molecules and the emergence of a chiral bias, Life **9**, 29 (2019).

[82] A. Jorissen and C. Cerf, Asymmetric photoreactions as the origin of biomolecular homochirality: A critical review, Origins Life Evol. Biospheres **32**, 129 (2002).

[83] G. Balavoine, A. Moradpour, and H. B. Kagan, Preparation of chiral compounds with high optical purity by irradiation with circularly polarized light, a model reaction for the prebiotic generation of optical activity, J. Am. Chem. Soc. **96**, 5152 (1974).

[84] J. J. Flores, W. A. Bonner, and G. A. Massey, Asymmetric photolysis of (RS)-leucine with circularly polarized ultraviolet light, J. Am. Chem. Soc. **99**, 3622 (1977).

[85] U. J. Meierhenrich, L. Nahon, C. Alcaraz, J. H. Bredehöft, S. V. Hoffmann, B. Barbier, and A. Brack, Asymmetric vacuum UV photolysis of the amino acid leucine in the solid state, Angew. Chem., Int. Ed. **44**, 5630 (2005).

[86] C. Meinert, S. V. Hoffmann, P. Cassam-Chenaï, A. C. Evans, C. Giri, L. Nahon, and U. J. Meierhenrich, Photonenergy-controlled symmetry breaking with circularly polarized light, Angew. Chem. Int. Ed. **53**, 210 (2014).

[87] A. Zangwill, *Modern Electrodynamics* (Cambridge University Press, Cambridge, 2013).

[88] J. Perczel, J. Borregaard, D. E. Chang, H. Pichler, S. F. Yelin, P. Zoller, and M. D. Lukin, Photonic band structure of two-dimensional atomic lattices, Phys. Rev. A **96**, 063801 (2017).

[89] J. Perczel, J. Borregaard, D. E. Chang, H. Pichler, S. F. Yelin, P. Zoller, and M. D. Lukin, Topological quantum optics in two-dimensional atomic arrays, Phys. Rev. Lett. **119**, 023603 (2017).

Correction: Minor errors in the inline expression following Eq. (3) have been fixed.